Cement & Concrete Composites 34 (2012) 468–477

Contents lists available at SciVerse ScienceDirect

Cement & Concrete Composites

journal homepage: www.elsevier.com/locate/cemconcomp

Measurement of elastic properties of calcium silicate hydrate with atomic force microscopy

Christopher A. Jones [a], Zachary C. Grasley [a,*], James A. Ohlhausen [b]

[a] Zachry Department of Civil Engineering, Texas A&M University, College Station, TX 77845, United States
[b] Sandia National Laboratories[1], PO BOX 5800, MS 0886, Albuquerque, NM 87185, United States

ARTICLE INFO

Article history:
Received 22 April 2011
Received in revised form 17 November 2011
Accepted 18 November 2011
Available online 25 November 2011

Keywords:
Contact mechanics
AFM
Atomic force microscopy
Nanoindentation

ABSTRACT

Atomic force microscopy (AFM) based indentation is compared to conventional nanoindentation for measuring mechanical properties of cement pastes. In evaluating AFM as a mechanical characterization tool, various analytical and numerical modeling approaches are compared. The disparities between the numerical self-consistent approach and analytical solutions are determined and reported. The measured elastic Young's modulus determined from AFM indentation tests are compared to elastic Young's modulus determined from nanoindentation tests of cement paste. These results indicate that the calcium silicate hydrate (C–S–H) phase of hydrated Portland cement has different properties on the different length scales probed by AFM versus nanoindenters. Packing density of C–S–H particles is proposed as an explanation for the disparity in the measured results.

1. Introduction

Nanoscale mechanical characterization of Portland cement paste has yielded interesting new findings about this ubiquitous construction material but has also raised many questions as well. Nanoindentation has long been the method of choice for micromechanical characterization of a variety of materials [1–5], but when applied to cementitious materials, the interpretation of the measured results are complicated by the somewhat ambiguous nanometric structure of Portland cement paste. Specifically in question is the source of the multimodal distribution of measured properties reported in virtually every nanoindentation based study of Portland cement paste [6–16].

The source of the multimodal distribution of measured mechanical properties could be attributed to distinct levels of packing density in the C–S–H phase as proposed by Ulm and co-authors [9,10,12,14–18] or the distribution of measured mechanical properties could be attributed to stiffer crystalline phases present in the C–S–H phase as proposed by Trtik et al. [19,20]. Both explanations are tractable and have basis in well established existing theories. The packing density explanation owes to the colloidal model for C–S–H first proposed by Powers [21] and then later developed by Jennings and coworkers [12,22–26]. Similarly, crystalline hydration products have long been known to exist in hydrated Portland cement [27] and the mechanical properties of the crystalline phases do differ from those of the C–S–H phase [28]. Chen et al. provided additional support for the presence of nanometric crystalline phases within C–S–H that could influence nanoindentation results [16]. It should be noted that neither explanation necessarily excludes the other and that the debate on this topic has mainly centered on determining the most likely explanation for the mostly undisputed experimental results.

Atomic force microscopy (AFM) can illuminate this discussion to some degree because it interacts with a smaller volume of material than is typical of nanoindentation experiments.[2] A reduction in interaction volume should reduce the porosity in the interaction volume and the probability of other phases residing with the interaction volume, causing the measured values to approach those of the intrinsic C–S–H particles. The measurement of mechanical properties with AFM is not a new idea, but obtaining consistent, accurately calibrated properties from AFM based indentation experiments has proven difficult. Furthermore, since nanoindentation produces perfectly acceptable results for homogeneous materials, the added complexity of AFM based measurements makes AFM based indentation less appealing for large classes of materials. Nevertheless, given the heterogeneous structure of C–S–H on the micron to nanometer

* Corresponding author. Tel.: +1 979 845 9961; fax: +1 979 458 0780.
E-mail addresses: cajone@sandia.gov (C.A. Jones), zgrasley@civil.tamu.edu (Z.C. Grasley), jaohlha@sandia.gov (J.A. Ohlhausen).

[1] Sandia National Laboratories is a multi program laboratory managed and operated by Sandia Corporation, a wholly owned subsidiary of Lockheed Martin Corporation, for the US Department of Energy's National Nuclear Security Administration under Contract DE-AC04-94AL85000.

[2] In this paper, the term 'nanoindentation' will refer strictly to experiments performed using a traditional nanoindenter (e.g. with a Berkovich indenter tip and μN force range).

0958-9465/$ - see front matter © 2011 Elsevier Ltd. All rights reserved.
doi:10.1016/j.cemconcomp.2011.11.008

scale, useful and distinct information can be gained from AFM that is not garnered from nanoindentation.

AFM based characterization of Portland cement paste has been initiated by various researchers. Mondal et al. performed nanoindentation experiments coupled spatially with AFM to correlate various results with particular morphological phases [29]. Similarly, Saez De Ibarra et al. used AFM and nanoindentation to characterize cement paste with carbon nanotube dispersions [30]. More recently, Kim et al. used atomic force acoustic microscopy to quantify the elastic properties of Portland cement paste [31]. However, none of these approaches use the AFM probe as one would use a nanoindenter to extract a force versus displacement curve to characterize the material elastic properties.

The objectives of this study are to address the interpretation of AFM indentation data and provide insight into the application of various approaches for modeling AFM indentation as applied to cement paste. Additionally, the elastic properties of C–S–H will be experimentally measured on the tens-of-nanometers length scale with AFM and these measurements will be used to help illuminate the discussion surrounding the multi modal distribution of C–S–H mechanical properties measured with nanoindentation.

2. Theory

The theory that is used to model indentation tests generally arises out of the field of contact mechanics where two arbitrarily shaped bodies interact with one another. Indentation is also similar to the Boussinesq problem of a rigid foundation interacting with an elastic half space. The primary difference between the classic analytical contact theories is the geometry of the body interacting with the elastic half space. More recently, numerical approaches have been proposed that avoid some of the simplifying assumptions present in the analytical theories.

2.1. Classic analytical approaches

The two most common contact theories regularly in use are the Hertz and Sneddon theories and the major difference in these theories involves the assumed geometry of the contact, or for indentation, the assumed shape of the indenter being used to press into the material and the related pressure field in the contact area. In the case of Hertzian indentation, the indenter is a half sphere of radius R [32]. The central equation of the Hertz solution that relates indentation depth to load may be cast as

$$F = \frac{4}{3} M R'^{/2} \delta^{3/2}, \tag{1}$$

where F is the load applied to the spherical indenter, δ is the indentation depth, and M is the indentation modulus expressed as

$$\frac{1}{M} = \frac{1 - \nu^2_{\text{material}}}{E_{\text{material}}} + \frac{1 - \nu^2_{\text{indenter}}}{E_{\text{indenter}}}, \tag{2}$$

where E is the elastic Young's modulus, ν is the Poisson's ratio, and the subscripts denote whether the property is of the indenter or of the material being indented. For diamond indenters ($E \sim 1$ TPa), the second term in (2) is often negligible such that

$$M \approx \frac{E_{\text{material}}}{1 - \nu^2_{\text{material}}} = \frac{E}{1 - \nu^2}. \tag{3}$$

In traditional nanoindentation and with many AFM probes, pyramidal indenters are the norm and can be idealized as conical. The Galin–Sneddon solution is appropriate for these experiments and the solution for conical indentation can be cast as

$$F = \frac{2M \tan(\phi)}{\pi} \delta^2, \tag{4}$$

where ϕ is the half angle of the conical indenter probe [33,34]. Eqs. (1) and (4) can be used to fit experimental force versus displacement data and determine M for the indented material.

2.2. Surface forces

Classical contact mechanics has adequately described the interaction and deformation between bodies in the cases of micro and nanoindentation for many years, but with the increase in popularity of AFM, new questions have been raised regarding the applicability of classical solutions to the AFM contact problem. Since the attractive forces measured with AFM are often approximately the same order of magnitude as those applied to the AFM probe, ignoring adhesive surface forces may result in significant error. Fig. 1 schematically shows a generalized contact scenario and a generalized indentation scenario. For two axisymmetric bodies or for an axisymmetric indenter and a flat surface, the separation between the bodies h varies as a function of the radial coordinate r. For most materials, the combination of varied surface separation as a function of position and general surface physics causes the indenter probe to experience both attractive and repulsive forces while in contact. While separation dependent surface forces do exist in micro and nanoindentation experiments, generally the load applied to the indenter tip is so much larger than the contribution of the adhesive surface forces that the surface forces can simply be neglected. The bodies experience various surface forces which in aggregate can often be adequately described by the empirical Lennard–Jones potential function [35].

The Lennard–Jones model proposes that the two bodies in question experience negligible surface forces at large separations, attractive surface forces at intermediate separations, and repulsive surface forces at very small separations (what would generally be known as "in contact"). The Lennard Jones equation can be cast as

$$p_s(h) = \frac{A}{6\pi h^3} \left[\left(\frac{z_0}{h}\right)^{12} - \left(\frac{z_0}{h}\right)^{6} \right], \tag{5}$$

where $p_s(h)$ is the pressure profile between the two bodies as a function of surface separation h, z_0 is the equilibrium separation distance, and A is Hamaker's constant, which can be related to the interfacial surface energy of the interacting bodies according to

$$\gamma = \frac{A}{16\pi z_0^2}. \tag{6}$$

For the purposes of this study, γ is not precisely the intrinsic interfacial surface energy of the interacting indenter and substrate; rather, it is a sum of surface energy, meniscus forces, and electrochemical forces. The Lennard–Jones expression has the advantage of describing both the attractive and repulsive phenomena known to exist in contact mechanics of most materials. For minimally adhesive materials, or for large indentation depths where the adhesive contribution to the total force is minimal compared to the repulsive contribution, a simpler Poisson–Boltzman repulsion form may be more appropriate [36]. The exponential repulsive form considered here is

$$p_s(h) = P_r \exp(-\kappa h) + P_r \left(\frac{z_0}{h}\right)^9, \tag{7}$$

where P_r controls the magnitude of the pressure while κ and z_0 control the separation at which the interaction takes place. The term z_0 is taken to be small so that the second term in (7) dominates the pressure response at small separations and prevents negative values of h from being encountered in the simulation.

Two primary analytical theories exist that account for the influence of adhesive surface forces on the contact problem. The solution proposed by Johnson, Kendall, and Roberts (JKR) [37] accounts for

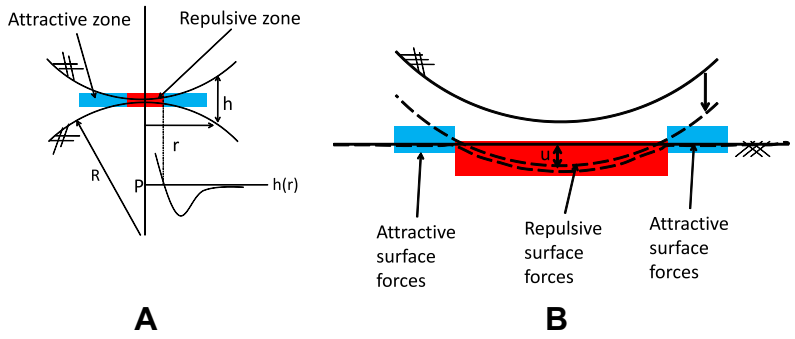

Fig. 1. (A) As two arbitrary bodies come into contact, separation dependent surface forces (assumed to obey a Lennard–Jones form) dictate that there must be a region of repulsive action and an attractive region. The forces are a function of separation between the bodies which is in turn a function of radial position for curved bodies. (B) In the case of indentation, the force applied to the indenter body deforms the material being indented and the area of repulsive surface forces grows as the contact area increases while the attractive zone remains roughly constant.

adhesion within the area of contact while the solution proposed by Derjaguin, Muller, and Toporov (DMT) [38] considers adhesion outside the area of contact. Both the JKR and DMT theories account for the effect of adhesive surface forces but both do so while making assumptions about the region of contact and the pressure profile between the interacting bodies. Furthermore, both theories are applicable to spherical contact which does not generally extend well to conical indenters. Also, neither theory describes the interaction between bodies in the pre-contact regime.

2.3. Numerical approaches

A few numerical solution approaches have been formulated for modeling contact problems. The solution proposed by Paul and Hashemi focused on accounting for nonspherical geometries often encountered in real engineering problems and was solved by assuming positive pressure within the "contact area" and zero pressure outside [39,40]. Another method proposed by Kalker involves minimizing elastic strain energy by iterating pressure and deformation profiles and also assumes no interaction outside the contact area [41]. A more recent numerical solution method was proposed by Attard that makes fewer assumptions and is therefore considered to be potentially more accurate [42–46]. Attard's method assumes small deformation gradients and linear elasticity apply, and that all displacements occur strictly along the axis of the indenter motion.

2.4. Attard's self-consistent method

Attard's self-consistent approach involves modeling the surface forces such that their affect on the indenter pressure profile is separation distance dependent [42,43]. In other words, the axisymmetric pressure profile between the indenter and the material being investigated is

$$p_s(r) = p_s(h(r)), \tag{8}$$

where p_s is the surface pressure profile and $h(r)$ is the separation between the surfaces at a radial coordinate r. Furthermore, the separation of the surfaces can be determined by subtracting the surface displacement $u(r)$ from the separation expected if the motion were considered rigid, such that

$$h(r) = h_0(r) - u(r), \tag{9}$$

where $h_0(r)$ is the rigid separation (negative indicating interpenetration of the original undeformed surfaces) for the two surfaces. The surface displacement may be expressed as

$$u(r) = -\frac{1}{\pi M}\int \frac{p_s(h(s))}{|r-s|}ds, \tag{10}$$

where ds is the element of the area over which the integration takes place, and s is simply a spatial variable in the plane that bisects the axis of contact.

The self-consistent approach conceptually mimics a displacement controlled indentation experiment. The method begins with the indenter and the material far apart such that no surface force is expected. In this initial state it is assumed that

$$\begin{aligned} u(r) &= 0, \\ h(r) &= h_0(r). \end{aligned} \tag{11}$$

Then, the indenter makes one small step toward the material such that the new $h_{0new} = h_{0old} + \Delta$, where Δ is small (on the order of 10^{-10}–10^{-12} m). With a new h_0 a new displacement, $u(r)$, is *guessed* according to

$$u(r)_{\text{guess}} = h_0(r)_{\text{new}} - h(r)_{\text{old}}. \tag{12}$$

With the guessed displacement, a new separation, $h(r)$, can be calculated with (9) and a new pressure profile can be calculated with (8) and either (5) or (7). With a new pressure profile, a new displacement, $u(r)$, can be *calculated*. This calculated displacement profile is then blended with the guessed displacement from (12) at a prescribed mixing ratio to create a new "guessed" displacement profile and the loop is started anew. For each h_0 step, this loop will continue until the difference between the newly calculated displacement profile and the previously guessed displacement profile differ by a small amount (1×10^{-12} m in this study). Once the error in the deformation is minimized, a new h_0 step is made and the process is repeated for each successive h_0 step. This process is illustrated in Fig. 2 in flow chart form.

The self-consistent numerical method yields many advantages and some disadvantages over analytical solutions. First, $h(r)$, $u(r)$, and $p_s(h(r))$ are determined (and recorded) at every step, in addition to simply recording the force. Recording these quantities yields a wealth of information that is not available in the analytical solutions. However, the major problem with this method is the computational expense required to arrive at a solution. Since each incremental step must be iterated to find the correct displacement and separation, the process can be computationally expensive. Additionally, the value of Hamaker's constant is generally not known a priori for most materials. Drawbacks aside, the Attard method of modeling the contact between two bodies is the most general approach currently in use. Both the Attard method and the analytical methods discussed in this paper are subject to inherent error based on the assumptions of material and geometric

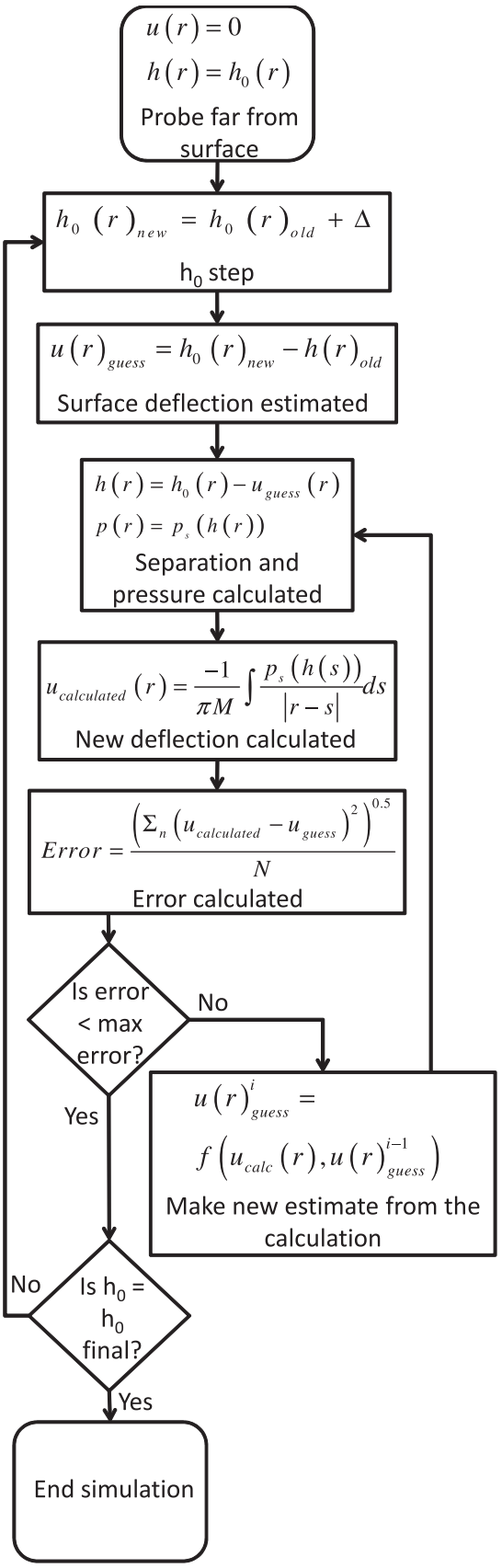

Fig. 2. A flow chart representing the self-consistent method [42] shows the equations and the routine for simulating an indentation experiment.

linearity presumed in all Hertzian-based contact theories. The assumption of linearity is a particular problem with sharp indentation probes such as are typical with AFM. The error associated with nonlinearity is acknowledged but not addressed in this work.

2.5. Advantages of the self-consistent method

As alluded to above, the self-consistent method has two primary practical advantages compared to traditional analytical techniques. First, given the generalization of the self-consistent method by Graham et al. [47], realistic tip geometries can be considered for any axisymmetric indenter shape. Second, realistic surface forces and their related pressure profiles can be considered. Fig. 3 shows a simulated indenter probe with a 40 nm tip radius and an included cone half angle of 48.5°, which represents a typical cube corner indentation probe.

The benefits of accurately accounting for the actual tip geometry in an indentation experiment depends on the particular experimental conditions, specifically, the indentation depth compared to the characteristic geometry of a particular tip. For example, if a spherical indenter is displaced to a depth much less than the radius of the spherical tip, then the geometric assumptions of the Hertz solution are perfectly acceptable [48,49]. Similarly, if a cono-spherical tip is indented such that the depth of penetration is much greater than the radius of the conical tip, then the geometric assumptions of the Sneddon solution are suitable [50]. An advantage of the self-consistent method is that the geometry of the contact is accounted for at any indentation depth.

With AFM based indentation, one approach has been to use relatively large spherical probes with low applied forces in an effort to meet the conditions of the Hertz solution [46]. This approach unfortunately neutralizes one of the great advantages of AFM, which is the extremely small tip dimensions available and the potential for measuring properties of adjacent dissimilar materials. By accurately accounting for the tip geometry of sharp AFM probes, one retains the ability to extract accurate material properties from very small areas of a material sample. For large classes of materials such as composites and naturally heterogeneous materials like Portland cement paste, the material properties can vary on short length scales of the same relative magnitude as the tip dimensions.

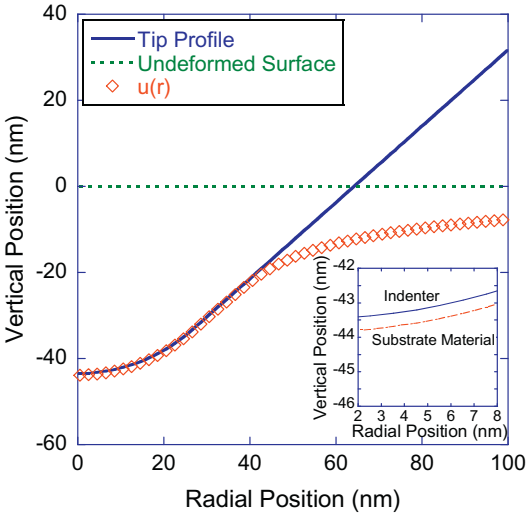

Fig. 3. The idealized cono-spherical tip geometry representing a diamond cube corner probe at $h_0 = 42$ nm generated with the self-consistent solution. The inset shows that the surfaces never "touch" with realistic separation dependent surface forces.

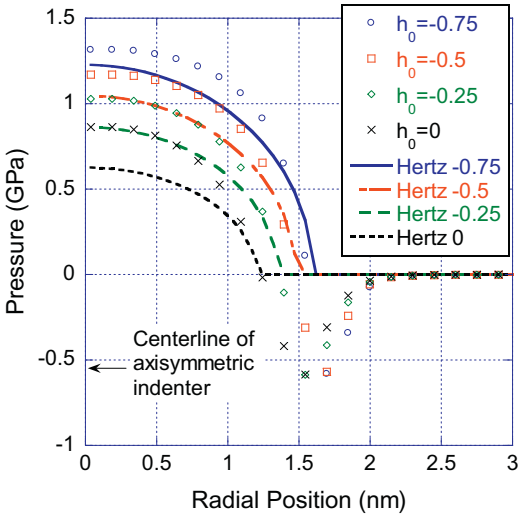

Fig. 4. The simulated pressure profiles for an AFM probe with tip radius 2 nm at several indentation depths show the ability of the self-consistent solution to capture both repulsive and adhesive effects. Also plotted are the Hertzian pressure profiles for the same indentation depths. Notice that because the Hertz solution neglects the adhesion outside the area of contact, the overall magnitude of the pressure profile is reduced to achieve an equivalent total applied force.

The second major advantage of the self-consistent approach is the flexibility in the pressure profile between the indenter and the material. For the Boussinseq problem to be analytically solved, a mathematical form of a pressure profile must be assumed. For example, in the case of the Hertz solution, the pressure is of the form of an ellipse such that

$$P_s(r) = P_0\left(1 - \frac{r^2}{a^2}\right)^{1/2}, \tag{13}$$

where P_0 is the maximum pressure and a is the radius of the circular "contact area". The first major advantage of accurate geometric accounting is also related to the second major advantage through the concept of contact area in the analytical expression of $p(r)$ given in (13). As is expected from an understanding of realistic surface forces, the two surfaces in contact never actually "touch."[3] This separation between the two surfaces, even at positive applied force levels, is preserved in the self-consistent solution and is shown in the inset in Fig. 3. Since the self-consistent method only predefines the pressure–separation relationship, this allows for a more general $p_s(h(r))$ and, as a result, a more general solution to the contact problem.

Fig. 4 shows the calculated pressure profiles at multiple indentation depths determined from a simulated experiment with a typical silicon AFM imaging probe and Portland cement paste. It is interesting to note that as the indentation depth increases, the shape of the pressure profile changes to match the shape of the indenter, since the repulsive contribution dominates the $p_s(h(r))$ response. Also plotted in Fig. 4 is (13) plotted at the same indentation depths with a assumed to equal the r position corresponding to the inflection point of the numerically generated pressure profile. The particular P_0 values chosen for the solid curves in Fig. 4 were determined by matching the total force applied to the indenter probe. Since the Hertz solution does not account for adhesive surface pressure clearly shown, the peak repulsive pressure in the Hertzian case is lower than that generated by the self-consistent solution.

[3] In continuum mechanics, the idea of "contact" is ambiguous since bodies are assumed to be comprised of points having no dimension, but no two points are allowed to coexist in the same space.

2.6. Applicability of the self-consistent method

Since the self-consistent method must iterate each rigid body displacement step, and because the method simulates an indentation experiment given a set of input parameters, obtaining a best-fit representation of an arbitrary indentation experiment can be cumbersome. Given the computational expense needed to implement the self consistent method, particularly when compared with the relative simplicity of analytical solutions, one naturally questions when the extra effort is necessary. This subsection aims to identify conditions where the self consistent method of modeling AFM contact provides tangible benefit over analytical solutions.

As alluded to in the previous sections, the applicability of an analytical solution may depend on the particular experimental conditions, or conversely, the necessity of the more cumbersome self-consistent solution may depend on specific experimental conditions. With this in mind, several AFM indentation tests are modeled with both analytical solutions and the self-consistent method. First, Fig. 5 shows typical force (F) versus h_0 data from an AFM indentation test fitted with Hertz, Sneddon, and self-consistent models. These data were obtained with a diamond cube corner tip with an effective tip radius of 40 nm. The loads applied to the tip in this case are in the range of μN, which is roughly comparable to very low nanoindentation loads.

Best fit values for the Hertz and Sneddon solutions for the fit parameter M were coincidentally both found to be 42 GPa while the self-consistent solution yielded 45 GPa. Fig. 5 shows that for this experiment, the self-consistent model does not provide a substantially better description of the experiment than the analytical solutions.

The results in Fig. 5 should not be generalized, however, as the applicability of the self-consistent routine is highly dependent on the experimental conditions. Fig. 6 shows a typical indentation test performed on cement paste with a very small probe and a very shallow indentation depth. For these data, the probe has a tip radius of approximately 2 nm and the maximum force is in the tenths of nanonewtons.

The most noticeable improvement that the self-consistent approach gains over the analytical solutions is the description of the pre-contact behavior. The inset in Fig. 6 highlights the traditional contact region (i.e. $h_0 < 0$). Since the analytical contact theories are only defined in the repulsive contact regime, the pre-repulsive (adhesive force) region is not described in either the Hertz or the Sneddon theories. Furthermore in terms of fitted elastic indentation modulus, there is great disagreement between the models. The self-consistent model data shown in Fig. 6 was generated with $M = 5$ GPa, while the Hertz and Sneddon solutions yielded $M = 0.95$ GPa and $M = 10$ GPa, respectively, as best fit modulus values. Since neither analytical solution accounts for the relatively large affect of surface forces in this test, the error introduced by modeling with the analytical solutions is significant.

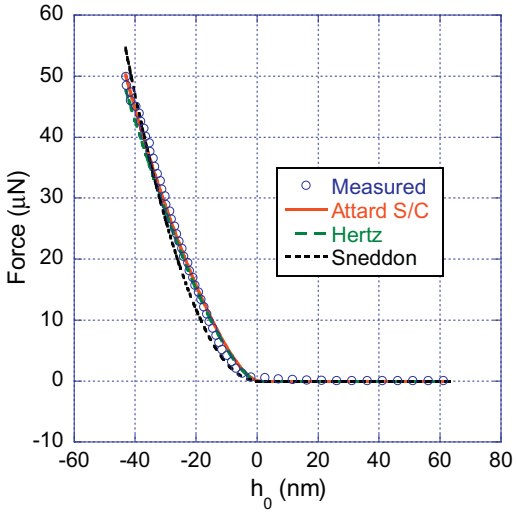

Fig. 5. AFM based indentation data for cement paste indented with a diamond cube corner probe are fitted with the self-consistent, Hertz, and Sneddon solutions. The data shown are obtained from the retraction of the probe from the hydrated cement surface to minimize incorporation of plasticity. The Hertz and self-consistent solutions are virtually identical for $h_0 < 0$.

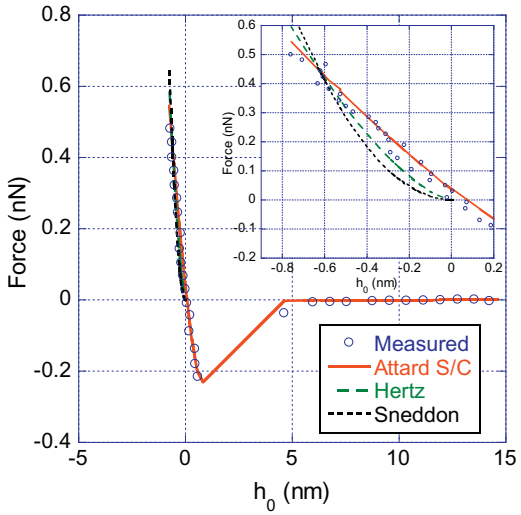

Fig. 6. Typical low force elastic indentation data obtained with a typical AFM imaging probe with tip radius ≈3 nm for very shallow indentation depth indicates the ability of the self-consistent solution to model the pre-contact behavior readily observed in AFM experiments. The inset shows the typical contact (e.g. $h_0 < 0$) regime that highlights the difference between self-consistent and analytical models.

Two cases have been shown where AFM obtained indentation data has been fitted with Attard's self-consistent solution and with traditional analytical solutions. For the data shown in Fig. 5, the benefit of using the self-consistent solution to model the experimental data is negligible, while for the data in Fig. 6 the self-consistent method is all but required. This section will conclude with an analysis of the relative accuracy of the analytical solutions versus the self-consistent method. A simple dimensionless parameter, θ, by which various test conditions can be compared was proposed by Fuller and Tabor [51] and Tabor [52] and will be modified slightly here. This parameter can simply be thought of as the force required to displace a given indenter to some depth in the material compared to the maximum adhesive pull off force exerted between that indenter and the material being tested, such that

$$\theta = \frac{F_{\text{indentation-peak}}}{F_{\text{attraction-peak}}}. \tag{14}$$

Specifically the terms in (14) can be substituted with (1) and (4) in the numerator, depending on the maximum indentation depth and the geometry of the tip used, while the denominator can be defined as

$$F_{\text{attraction-peak}} = 4\gamma\pi R, \tag{15}$$

where for this case, R is the radius of the spherical indenter tip or the radius of the tip of the conical–spherical indenter tip. Eq. (15) may be recognized as the adhesive pull off force term defined in [38]. For Hertzian indentation where the geometry is spherical or where the indentation is spherically dominated

$$\theta = \frac{M\delta_{max}^{3/2}}{3\gamma R^{1/2}} \tag{16}$$

and for Sneddon indentation where the indentation geometry is conically dominated

$$\theta = \frac{\delta_{max}^{2} M \tan(\phi)}{2\pi R\gamma}. \tag{17}$$

As a way of characterizing the error one might encounter from applying an analytical solution versus the self-consistent numerical solution, one may define

$$\text{Error}\% = \frac{|M_{fitted} - M_{simulation}|}{M_{simulation}} \times 100. \tag{18}$$

Fig. 7 represents the error in fitted M (determined via analytical solutions) compared to the same value from Attard's self-consistent numerical solution ($M_{simulation}$). The data points in this figure were created by generating combinations of M, δ_{max}, R, and γ that resulted in θ values that were spaced over a large range. Next, the self-consistent solution method was used to simulate indentation experiments with these combinations of input parameters and the force versus displacement data were exported and fitted with the Hertz, JKR, and DMT solutions to determine M_{fitted} using a nonlinear optimization routine in Mathematica. Finally, the error for a given θ was computed with (18).

Fig. 7 shows that for high values of θ the error introduced by modeling indentation experiments with analytical solutions is minimal, while as θ decreases the error increases rapidly. This is an important fact to note because the maximum indentation depth and the tip geometry can be selected when designing the experiment. It is also interesting to note that for these simulated indentation tests, neither the JKR nor the DMT theories produce tangible benefit compared to the Hertz theory, though for traditional contact mechanics applications such as determining the contact area between bodies, the JKR and DMT theories may provide more benefit. In general, for $\delta = 0$ both the JKR and DMT theories over predict the adhesive force compared to the self-consistent simulation. For experimental conditions where θ must be small such as very shallow indentation depth or very low modulus or high surface energy materials, numerical modeling such as the Attard self-consistent method should be employed to achieve accurate results.

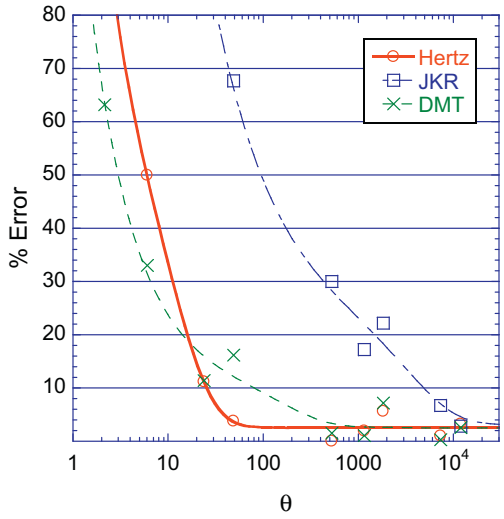

Fig. 7. As θ decreases, the error introduced by using the analytical solutions rapidly increases. Since some of the parameters that define θ are experimentally controllable, AFM based indentation experiments can be designed such that minimal error is introduced by modeling with analytical solutions.

3. Experimental

3.1. Materials

The specimens used in this study were cast from a typical Type I/II cement with a *w/c* of 0.4. The cement and water were mixed according to ASTM C305-99 and the resultant paste was placed into acrylic tubes with a square cross-section and an inner dimension of 1 cm (0.394 in.). On one end, an acrylic plate was affixed with a two-part epoxy. The length of the tubes was approximately 10 cm (3.94 in.). The fresh paste filled molds were vibrated and vacuumed to remove any entrapped air. The specimens were then sealed and placed into a 98% relative humidity room at a temperature of 23 °C for 24 h. Once the initial curing had taken place, the specimens were carefully demolded and placed in lime water for approximately 90 days.

The cured "beams" were radially sliced across the long axis of the beam into 3 mm thick 1 × 1 cm^2 plates using an Isomet precision wet saw. The slices were allowed to dry in the laboratory environment and were then affixed with cyanoacrylate glue to circular steel discs measuring 15 mm (0.591 in.) in diameter. The exposed flat surface of the cement paste sample was polished using techniques similar to those presented in [53], with the addition of final polishing using diamond slurries in five steps with diamond particle sizes ranging from 6 μm to 0.25 μm. In these final steps the diamond slurry was placed on a glass plate and the specimen was manually oscillated against the glass. After each diamond slurry polishing step the specimen was wiped dry with denatured alcohol to remove any residue from the slurry.

3.2. Atomic force microscopy

Fig. 8 schematically illustrates the concept of AFM based indentation. As the actuator presses the probe tip into the material, the cantilever bends upward and the difference in these displacements is interpreted as the penetration depth. Additionally, if the stiffness of the cantilever is known, the deflection of the end of the cantilever also defines the force applied to the tip.

The AFM based indentation experiments in this study were performed with a Veeco Dimension Icon AFM. In concept, the experiment is identical to the nanoindenter based experiment but with a few key procedural differences that are inherent to the atomic force microscope. First, the deflection sensitivity of the cantilever

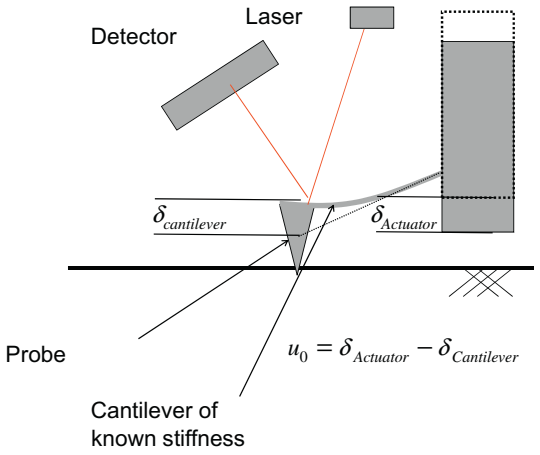

Fig. 8. A schematic representation of an atomic force microscopy probe shows the deflection of the cantilever being generated by the movement of the base of the cantilever. The deflection of the cantilever and the movement of the actuator define the penetration depth δ of the AFM probe.

used must be determined. Second, the spring constant or k value must also be obtained for the cantilever. The calculated value of deflection sensitivity is obtained by deflecting the cantilever against a very stiff material such that negligible deformation of the surface can be expected and all of the movement of the actuator is directly related to deflection of the cantilever. For these experiments a calibrated cantilever was used that had a k value of 219 N/m. It should be noted that the deflection sensitivity is dependent on the mounting of the cantilever and alignment of the internal laser in the atomic force microscope and therefore should be calibrated each time an experiment or batch of experiments is performed. Finally, the tip of the diamond cube corner probe was scanned across a polycrystalline titanium reference sample to calibrate the tip shape. With the Veeco supplied tip shape deconvolution routine, the tip radius was found to be approximately 40 nm which is in good agreement with the tip specifications. For these AFM based experiments the indentation depth averaged 36.6 nm such that only the spherical tip of the otherwise pyramidal indenter probe interacted with the sample.

Since the cantilever deflection values are calculated based on changes in photodiode voltage values from a baseline, the resultant data must be shifted to accurately match the zero force and zero indentation depth points of the curve. This is done by simply setting an offset to the indentation depth and to the applied force data to accurately shift the origin of the plot to the correct point. This correction is necessary simply due to the inherent design of the atomic force microscope.

For this work, 5×5 grids of indentation points were performed at 8 different randomly selected locations on the surface of the cement paste specimen.

4. Results

4.1. Measured results

As noted previously, a total of 200 AFM based indentations were performed at various locations on the cement paste sample as well as 44 traditional nanoindentation tests, originally presented in [17]. Since the θ value associated with the AFM indentation tests was approximately 1000 on average, the retraction portion of each test was fitted with (1) to determine M and a value of $\nu = 0.2$ was assumed to calculate E from (3). Fig. 9 shows a histogram of the measured elastic Young's moduli from the AFM indentation tests along with the comparable results obtained from nanoindenatation.

It is interesting to note in Fig. 9A that the distribution appears to be bimodal in nature as opposed to the multimodal distribution obtained via nanoindentation as suggested in recent literature [16,22] and in Fig. 9B. It is also interesting to note that the average value of E extracted from the AFM tests is higher than that measured with nanoindentation.

Two plausible explanations exist in the literature for the modality of the distribution of elastic properties measured with indentation tests. The first plausible explanation of the modality of E obtained from indentation tests can be gleaned from the colloidal model for C–S–H. This model proposes small spherical particles as the basic building block of C–S–H. According to the model, these particles flocculate into larger, roughly spherical clumps that in turn flocculate into the C–S–H gel. Jennings [24] suggested that C–S–H particles are packed in two distinct densities: low density and high density forms. Based on Jennings' model, Ulm et al. [9,15,54] have suggested that there are a limited number of *distinct* packing densities (either 2 or 3) of the C–S–H particles, with each distinct packing density reflecting a peak in the measured Young's modulus determined through nanoindentation. The second plausible explanation for the modality of measured E is related to the presence of multiple phases (i.e. C–S–H with other phase(s)) within the interaction volume of the indentation test [19,20]. Either proposed mechanism (alone or in concert) could explain the observed modality in nanoindentation results.

However, there are distinct differences between the materials probed in the AFM test versus the nanoindenter test. Fig. 10 shows a typical AFM topography image of polished cement paste that indicates rounded particles grouped into clumps, which ostensibly supports the colloidal spheres model of C–S–H, since the spherical features observed in Fig. 10 are of similar size to the particles hypothesized in the colloidal spheres model. Furthermore, the clumps appear to have interspersed voids. In general, a topographical image from AFM does not have great intrinsic quantitative value other than for determination of morphology, but in this case, AFM images can be useful for providing insight into the interpretation

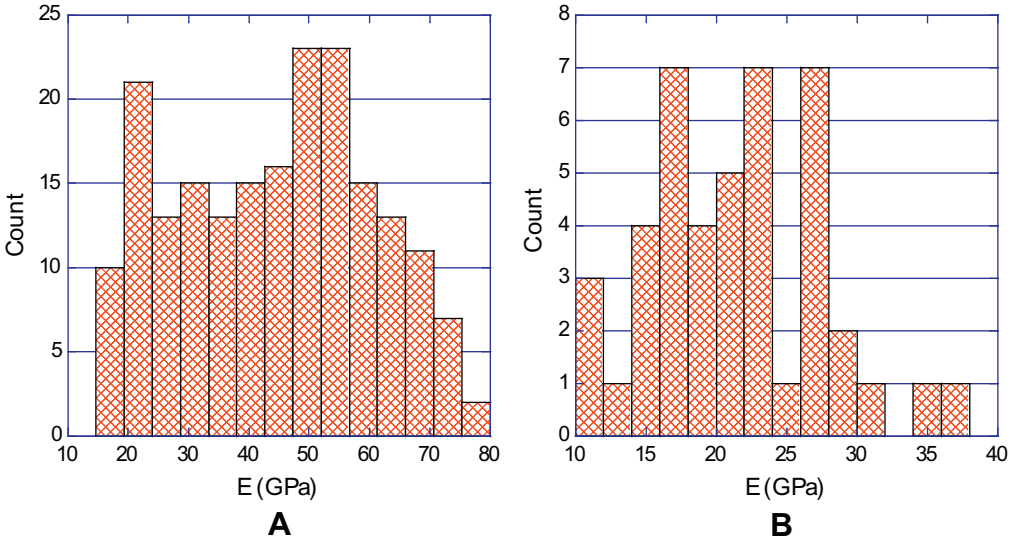

Fig. 9. (A) The elastic Young's modulus measured with AFM shows an apparent bimodal distribution while (B) Young's modulus measured with nanoindentation [17] shows a multimodal trend.

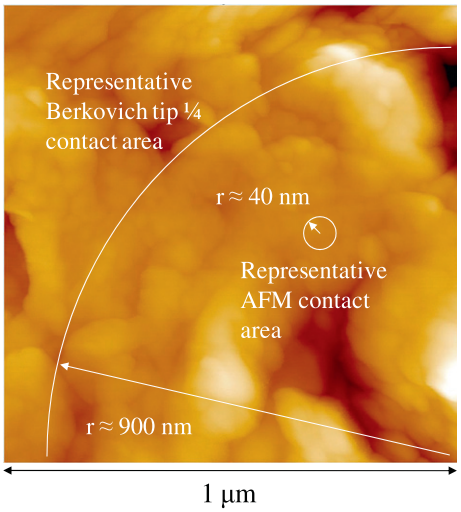

Fig. 10. A typical AFM topographical image of cement paste seems to support the colloidal structure of C–S–H. Inscribed on the image are representations of the approximate contact areas of the AFM probe and a typical nanoindentation probe at maximum indentation depth.

of the AFM indentation results. Fig. 10 shows scaled representations of the typical contact area between the indenter tip (AFM or nanoindenter) and the cement paste. The significant difference in typical contact area suggests that the nanoindenter is interacting with the larger length scale porosity while the AFM based indentations are not. As a result of this observation, it appears likely that the bimodal distribution of measured E with AFM compared to the multimodal distribution measured with the nanoindenter is explained by the increased influence of porosity when testing with nanoindentation. When comparing the results in Fig. 9A to analogous nanoindenter results in Fig. 9B and the literature [16,17], the peak missing from Fig. 9A appears to be that in the lowest stiffness range, which would correspond to interaction volumes containing larger porosity that is avoided in the AFM tests. It is possible that the AFM based indentation tests are resolving the "high density" and "ultra high density" phases of C–S–H.

The reduced influence of porosity on every AFM measurement versus nanoindentation measurement could also explain the general upward shift in measured E in AFM results versus nanoindentation results. While the presence of crystalline material in the otherwise amorphous C–S–H could still be an explanation for the distribution of measured nanoindentation results, this explanation is not as plausible for AFM indentation tests. Since the interaction volume of the AFM probe is quite small, the measured values are much less likely to involve influence from multiple phases and are thus likely more representative of the intrinsic properties of the C–S–H particles. Furthermore, the intrinsic E of C–S–H has been approximated as 57 GPa [55], 60 GPa [9], 80 GPa [56], and 34–300 GPa, depending on Ca^{2+} concentration [57]. Since the AFM results indicate E approaching 80 GPa, it is likely that the intrinsic E of C–S–H must be at least 80 GPa. Indeed, DEM simulations of nanoindentation using 57 GPa as an intrinsic E of C–S–H under predicted nanoindentation results [58]. If the intrinsic C–S–H E is greater than 80 GPa, then the existence of CH in place of C—S—H particles within the AFM interaction volume cannot explain the measured AFM indentation results that approach 80 GPa since the E of CH is (on average) approximately 40 GPa [28]. In addition, perhaps due to sample preparation, virtually no crystalline materials were readily observed on the surface (via AFM imaging) of the samples.

While the presence of unhydrated cement grains ($E \approx 118$ GPa [28]) in the AFM indentation interaction volume could theoretically explain the upper end of the measured E determined via AFM indentation, the very shallow AFM indentation depth greatly reduces the probability of interacting with unhydrated cement particles since the water used during cutting and polishing would ensure sufficient moisture for hydration of any exposed unhydrated cement particles. Furthermore, no indentation results approached the expected Young's modulus for unhydrated cement grains and no crystalline materials were identified during imaging. Therefore, it is hypothesized that the difference between the measured E obtained from nanoindentation and from AFM is due primarily to differences in particle packing between the two length scales. The reader is cautioned of the possibility that the increased particle packing is confined to the surface layer of the samples tested and is an artifact of the polishing process (i.e. the polishing may cause surface compaction of the C–S–H particles). Since AFM probes a much shallower depth than nanoindentation, it is likely that AFM would be more sensitive to surface polishing artifacts. However, even if the surface layer were artificially of higher packing density than the subsurface, this does not change the conclusion regarding the source of the differences in AFM and nanoindentation results as differences in packing density but rather speculates on the source of packing density differences.

5. Conclusions

Numerical and analytical modeling approaches are presented and considered for application to AFM based indentation tests, and the two approaches are compared to one another. The numerical approach is considered more general but significantly more computationally intensive. By evaluating a dimensionless parameter θ, the applicability of the analytical techniques can be determined and future experiments may be designed such that analytical modeling is suitable and the computational expense of numerical modeling avoided. For many cases, including the experiments performed in this study, analytical techniques prove sufficiently accurate for modeling indentation on small length scales.

Quantitative AFM based indentation experiments have been performed on Portland cement paste and measured Young's moduli values of the C–S–H phase have been reported. The mean and distribution of the measured values obtained from AFM indentation are distinct from the measured values obtained with nanoindentation both in average value and in distribution. Particle packing density considering a colloidal spheres structure for C–S–H seems to provide the best framework for reconciling the differences between the AFM results and those obtained with nanoindentation.

Acknowledgements

This research was supported by the National Science Foundation CAREER Award Program under Grant Number CMMI-0843979. Any opinions, findings, and conclusions or recommendations expressed in this material are those of the author(s) and do not necessarily reflect the views of the National Science Foundation.

References

[1] Ulm FJ, Vandamme M, Bobko C, Alberto Ortega J, Tai K, Ortiz C. Statistical indentation techniques for hydrated nanocomposites: concrete, bone, and shale. J Am Ceram Soc 2007;90(9):2677–92.
[2] Bobko C, Ulm F-J. The nano-mechanical morphology of shale. Mech Mater 2008;40(4–5):318–37.
[3] Velez K, Maximilien S, Damidot D, Fantozzi G, Sorrentino F. Determination by nanoindentation of elastic modulus and hardness of pure constituents of Portland cement clinker. Cem Concr Res 2001;31(4):555–61.
[4] VanLandingham M, Villarrubia J, Guthrie W, Meyers G. Nanoindentation of polymers: an overview 2001; 15–44.
[5] Nemecek J, Smilauer V, Kopecky L, Nemeckova J. Nanoindentation of alkali activated fly ash. Transport Res Rec 2010;1(2141):36–40.

[6] Zhu W, Hughes JJ, Bicanic N, Pearce CJ. Nanoindentation mapping of mechanical properties of cement paste and natural rocks. Mater Charact 2007;58(11–12 SPEC. ISS.):1189–98.
[7] Garas V, Jayapalan AR, Kahn LF, Kurtis KE. Multi-scale investigation of the effect of thermal treatment on the tensile creep of ultra-high performance concrete: preliminary assessment. Int J Mater Struct Integrity 2009;3(2–3):187–200.
[8] Garas VY, Jayapalan AR, Kahn LF, Kurtis KE. Micro- and nano-scale characterization of effect of interfacial transition zone on tensile creep of ultra-high-performance concrete. Transport Res Rec 2010(2141):82–8.
[9] Ulm FJ, Constantinides G. The nanogranular nature of C–S–H. J Mech Phys Solids 2007;55(1):64–90.
[10] Sorelli L, Constantinides G, Ulm F-J, Toutlemonde F. The nano-mechanical signature of ultra high performance concrete by statistical nanoindentation techniques. Cem Concr Res 2008;38(12):1447–56.
[11] Mondal P, Shah SP, Marks L. A reliable technique to determine the local mechanical properties at the nanoscale for cementitious materials. Cem Concr Res 2007;37(10):1440–4.
[12] Jennings HM, Thomas JJ, Gevrenov JS, Constantinides G, Ulm F-J. A multi-technique investigation of the nanoporosity of cement paste. Cem Concr Res 2007;37(3):329–36.
[13] Hughes JJ, Trtik P. Micro-mechanical properties of cement paste measured by depth-sensing nanoindentation: a preliminary correlation of physical properties with phase type. 2 ed. Trondheim: Norway: Elsevier Inc.; 2004. p. 223–31.
[14] Constantinides G, Ulm FJ, Van Vliet K. On the use of nanoindentation for cementitious materials. Mater Struct 2003;36(257):191–6.
[15] Constantinides G, Ulm F-J. The effect of two types of C–S–H on the elasticity of cement-based materials: Results from nanoindentation and micromechanical modeling. Cem Concr Res 2004;34(1):67–80.
[16] Chen JJ, Sorelli L, Vandamme M, Ulm F-J, Chanvillard G. A coupled nanoindentation/SEM-EDS study on low water/cement ratio Portland cement paste: Evidence for C–S–H/$Ca(OH)_2$ nanocomposites. J Am Ceram Soc 2010;93(5):1484–93.
[17] Jones CA, Grasley ZC. Short-term creep of cement paste during nanoindentation. Cem Concr Compos 2010;33(1):12–8.
[18] Jennings HM, Thomas JJ, Gevrenov JS, Constantinides G, Ulm F-J. Reply to discussion of the paper "a multi-technique investigation of the nanoporosity of cement paste". Cem Concr Res 2007;37(9):1374–5.
[19] Trtik P, Munch B, Lura P. A critical examination of statistical nanoindentation on model materials and hardened cement pastes based on virtual experiments. Cem Concr Compos 2009;31(10):705–14.
[20] Lura P, Trtik P, Münch B. Validity of recent approaches for statistical nanoindentation of cement pastes. Cem Concr Compos 2011;33(4):457–65.
[21] Powers T. The physical structure in Portland cement paste. Chem Cem 1964.
[22] Ulm F-J, Vandamme M, Jennings HM, Vanzo J, Bentivegna M, Krakowiak KJ, et al. Does microstructure matter for statistical nanoindentation techniques? Cem Concr Compos 2010;32(1):92–9.
[23] Tennis PD, Jennings HM. Model for two types of calcium silicate hydrate in the microstructure of Portland cement pastes. Cem Concr Res 2000;30(6):855–63.
[24] Jennings HM. Model for the microstructure of calcium silicate hydrate in cement paste. Cem Concr Res 2000;30(1):101–16.
[25] Jennings HM. Colloid model of C–S–H and implications to the problem of creep and shrinkage. Mater Struct 2004;37(265):59–70.
[26] Jennings H. Refinements to colloid model of csh in cement: Cm-II. Cem Concr Res 2008;38(3):275–89.
[27] Mindess S, Young JF, Darwin D. Concrete. 2nd ed. Upper Saddle River, NJ: Prentice Hall; 2003.
[28] Haecker CJ, Garboczi EJ, Bullard JW, Bohn RB, Sun Z, Shah SP, et al. Modeling the linear elastic properties of Portland cement paste. Cem Concr Res 2005;35(10):1948–60.
[29] Mondal P, Shah SP, Marks LD. Use of atomic force microscopy and nanoindentation for characterization of cemetitious materials at the nanoscale. 254 SP ed. Denver, CO, United states: American Concrete Institute; 2008. p. 41–56.
[30] Saez De Ibarra Y, Gaitero JJ, Erkizia E, Campillo I. Atomic force microscopy and nanoindentation of cement pastes with nanotube dispersions. 6 ed. Wiley-VCH Verlag; 2006. p. 1076–81.
[31] Kim J, Balogun O, Shah S. Atomic force acoustic microscopy to measure nanoscale mechanical properties of cement pastes. Transport Res Rec: J Transport Res Board 2010;2141(−1):102–8.
[32] Hertz H. On the contact of elastic solids. J Reine Angew Math 1881;92:156–71.
[33] Galin L, Sneddon I, Moss H. Contact problems in the theory of elasticity: Department of Mathematics, School of Physical Sciences and Applied Mathematics, North Carolina State College; 1961.
[34] Sneddon IN. Relation between load and penetration in axisymmetric Boussinesq problem for punch of arbitrary profile. Int J Eng Sci 1965;3:47–57.
[35] Jones J. On the determination of molecular fields. II. From the equation of state of a gas. Proc Roy Soc London Ser A. Contain Pap Math Phys Charact 1924:463–77.
[36] Carnie SL, Torrie GM. The statistical mechanics of the electrical double layer; 1984.
[37] Johnson KL, Kendall K, Roberts AD. Surface energy and the contact of elastic solids. Proc Roy Soc London Ser A. Math Phys Sci 1971;324(1558):301–13.
[38] Derjaguin BV, Muller VM, Toporov YP. Effect of contact deformations on the adhesion of particles. J Colloid Interface Sci 1975;53(2):314–26.
[39] Paul B, Abadan I. Contact geometry associated with arbitrary rail and wheel profiles. ASME; 1980. p. 93.
[40] Paul B, Hashemi J. Contact pressures on closely conforming elastic bodies. J Appl Mech 1981;48:543.
[41] Kalker J, Van Randen Y. A minimum principle for frictionless elastic contact with application to non-hertzian half-space contact problems. J Eng Math 1972;6(2):193–206.
[42] Attard P, Parker JL. Deformation and adhesion of elastic bodies in contact. Phys Rev A (Statistical Physics, Plasmas, Fluids, and Related Interdisciplinary Topics) 1992; 46(12): 7959–71.
[43] Attard P. Interaction and deformation of elastic bodies: origin of adhesion hysteresis. J Phys Chem B 2000;104(45):10635–41.
[44] Attard P. Interaction and deformation of viscoelastic particles. 2. Adhesive particles. Langmuir 2001;17(14):4322–8.
[45] Attard P. Interaction and deformation of viscoelastic particles: nonadhesive particles. Phys Rev E 2001;63(6):61604.
[46] Attard P. Measurement and interpretation of elastic and viscoelastic properties with the atomic force microscope. J Phys: Condens Matter 2007;19:473201.
[47] Graham MA, Grasley ZC, Abu al-Rub RK. The effect of atomic force microscope probe size on nanoindentation. Int J Mater Struct Integrity 2010(4):2–3.
[48] Johnson K. The correlation of indentation experiments. J Mech Phys Solids 1970;18(2):115–26.
[49] Johnson K. One hundred years of hertz contact. In: Archive: Proceedings of the institution of mechanical engineers 1847–1982, (vols. 1–196), vol. 196(1982); 1982. p. 363–78.
[50] Oliver W, Pharr G. Improved technique for determining hardness and elastic modulus using load and displacement sensing indentation experiments. J Mater Res 1992;7(6):1564–83.
[51] Fuller K, Tabor D. The effect of surface roughness on the adhesion of elastic solids. Proc Roy Soc London Ser A. Math Phys Sci 1975;345(1642):327–42.
[52] Tabor D. Surface forces and surface interactions. J Colloid Interface Sci 1977;58(1):2–13.
[53] Kjellsen KO, Monsøy A, Isachsen K, Detwiler RJ. Preparation of flat-polished specimens for SEM-backscattered electron imaging and X-ray microanalysis–importance of epoxy impregnation. Cem Concr Res 2003;33(4):611–6.
[54] Vandamme M. The nanogranular origin of concrete creep: a nanoindentation investigation of microstructure and fundamental properties of calcium-silicate-hydrates. Massachusetts Institute of Technology; 2008.
[55] Pellenq RJ-M, Vandamme H. Why does concrete set?: the nature of cohesion forces in hardened cement-based materials. Warrendale, PA, ETATS-UNIS: Materials Research Society; 2004.
[56] Fonseca P. Nanoindentation simulations to predict macroscale properties of cement. Minerals, Metals and Materials Society/AIME, 420 Commonwealth Dr., P. O. Box 430 Warrendale PA 15086 USA.
[57] Plassard C, Lesniewska E, Pochard I, Nonat A. Investigation of the surface structure and elastic properties of calcium silicate hydrates at the nanoscale. Ultramicroscopy 2004;100(3–4):331–8.
[58] Chandler MQ, Peters JF, Pelessone D. Modeling nanoindentation of calcium silicate hydrate. Transport Res Rec 2010;2(2142):67–74.